Soft Matter

PAPER

Cite this: *Soft Matter*, 2018, **14**, 9599

The effect of particle wettability on the stick-slip motion of the contact line

Dong-Ook Kim, Min Pack, Arif Rokoni, Paul Kaneelil and Ying Sun *

Contact line dynamics is crucial in determining the deposition patterns of evaporating colloidal droplets. Using high-speed interferometry, we directly observe the stick-slip motion of the contact line *in situ* and are able to resolve the instantaneous shape of the inkjet-printed, evaporating pico-liter drops containing nanoparticles of varying wettability. Integrated with *post-mortem* optical profilometry of the deposition patterns, the instantaneous particle volume fraction and hence the particle deposition rate can be determined. The results show that the stick-slip motion of the contact line is a strong function of the particle wettability. While the stick-slip motion is observed for nanoparticles that are less hydrophilic (*i.e.*, particle contact angle $\theta \approx 74^\circ$ at the water–air interface), which results in a multiring deposition, a continuous receding of the contact line is observed for more hydrophilic nanoparticles (*i.e.*, $\theta \approx 34^\circ$), which leaves a single-ring pattern. A model is developed to predict the number of particles required to pin the contact line based on the force balance of the hydrodynamic drag, interparticle interactions, and surface tension acting on the particles near the contact line with varying particle wettability. A three-fold increase in the number of particles required for pinning is predicted when the particle wettability increases from the wetting angle of $\theta \approx 74^\circ$ to $\theta \approx 34^\circ$. This finding explains why particles with greater wettability form a single-ring pattern and those with lower wettability form a multi-ring pattern. In addition, the particle deposition rate is found to depend on the particle wettability and vary with time.

Received 18th October 2018,
Accepted 3rd November 2018

DOI: 10.1039/c8sm02129e

rsc.li/soft-matter-journal

1. Introduction

The motion of the contact line during evaporation of thin films,[1–3] menisci,[4–9] and droplets[10–12] is important in natural and industrial processes from the drying of tear films[13,14] to coating and printing technologies.[15–18] The evaporation of a sessile drop often involves three distinct stages:[19–21] the constant contact area mode where the contact line is pinned, followed by the constant contact angle stage where the contact line depins, and finally the mixed mode where both the contact area and contact angle decrease. The addition of particles in evaporating colloidal drops enhances the pinning of the contact line due to the accumulation of particles along the drop edge induced by the evaporation-driven flows. For such cases, the decrease in contact angle due to evaporation is offset by the increase in contact angle caused by the protrusion of particles at the contact line,[20] resulting in delays in the second and third stages of evaporation and the well-known coffee-ring deposition.[10] Additionally, a self-pinning mechanism of colloids has been demonstrated at the contact line when a critical packing fraction is reached regardless of the particle size and initial volume fraction.[22] Alternatively, the stick-slip motion, *i.e.*, the repetition of the pinning and depinning of the contact line, has also been observed in evaporating droplets,[23–26] where the "slip" behavior is a result of the contact angle reaching its static receding value as the droplet evaporates. When the contact line depins, the droplet rapidly reaches its equilibrium contact angle as the contact line "slips" to its next equilibrium position and "sticks" there. As a result of the competition between friction and surface tension forces, the stick-slip motion of the contact line repeats itself until the drop fully evaporates, leaving multiring depositions of sessile drops[25,27–30] and capillary bridges,[4,31,32] as well as well-spaced strip patterns in dip coating applications.[5,33]

Particle wettability has been shown to play an important role in determining the deposition morphologies of colloidal drops. Anyfantakis *et al.*[34] showed that, for microliter sessile drops, both hydrophilic and hydrophobic particles form coffee-ring deposits at low concentrations. At high concentrations, however, the deposition transitions from a ring to a dome-like pattern with increasing particle hydrophobicity, due to enhanced self-assembly of hydrophobic particles forming a connected network that prevents them from being pushed to the drop edge. Alternatively, Shao *et al.*[35] have shown that copolymer particles that are less hydrophilic form ring patterns whereas more-hydrophilic silica particles yield spoke depositions owing to the increased capillary force with particle wettability, assuming that particles

Department of Mechanical Engineering and Mechanics, Drexel University, Philadelphia, PA, USA. E-mail: ysun@coe.drexel.edu; Fax: +1 (215)895-1478; Tel: +1 (215)895-1373

are adsorbed to the drop surface. However, because most colloidal drop deposition studies mainly rely on *post-mortem* analysis, it is still unclear how the particle wettability affects the contact line dynamics as the drop evaporates. This is particularly true for inkjet-printed, pico-liter colloidal drops where the evaporation time scale is much shorter than the particle diffusion time scale for either particle self-assembly or adsorption to the drop surface to occur.

In this study, we seek to bridge the gap between the particle wettability and the stick-slip motion of the contact line of inkjet-printed colloidal droplets using *in situ* observation of the evaporation process. High-speed interferometry, combined with *post-mortem* deposition profilometry, is used to obtain the instantaneous contact line motion, contact angle, drop volume, and particle volume fraction. Dilute aqueous inks containing monodispersed 20 nm carboxylate-modified (more hydrophilic) or carboxyl (less hydrophilic) polystyrene particles are used while other parameters are kept the same. The experimentally observed dependence of the stick-slip motion of the contact line on particle wettability is compared with model predictions of the number of particles required for pinning based on a force balance of particles at the contact line. The instantaneous particle deposition rates during the colloidal drop evaporation process for particles of varying wettability are also obtained. Integrating modeling and experiments, we correlate the particle wettability, contact line motion, and final deposition morphology of inkjet-printed evaporating colloidal drops.

2. Experimental methods

The custom-built printing setup shown in Fig. 1a consists of a piezoelectric drop-on-demand printer synchronized with side-view flash photography to ensure stable droplets jetted from a print head with an orifice diameter of 80 μm (MicroFab MJ-AL-01). The picoliter-sized droplets were formed *via* a pneumatic control device (MicroFab) and a waveform generator (JetDrive). The side-view imaging of the drop was conducted using a 12× Navitar lens on a SensiCam CCD camera in tandem with a halogen strobe light (PerkinElmer). The lighting, imaging and droplet jetting were synchronized with a delay generator (SRS DG645) to obtain droplets of ≈60 μm diameter. The droplets were printed onto cleaned glass slides (Chemglass), which were also made more hydrophilic by plasma cleaning (2 minutes of air plasma at 18 W and 250 mTorr, Harrick Plasma PDC-32G). The equilibrium contact angle of water on plasma-cleaned glass substrates was measured to be close to 0° using a custom-built goniometer and the LB-ADSA drop analysis plugin of ImageJ (http://rsbweb.nih.gov/ij/). The relative humidity was controlled using an environmental chamber and the ambient temperature was maintained at 22 °C.

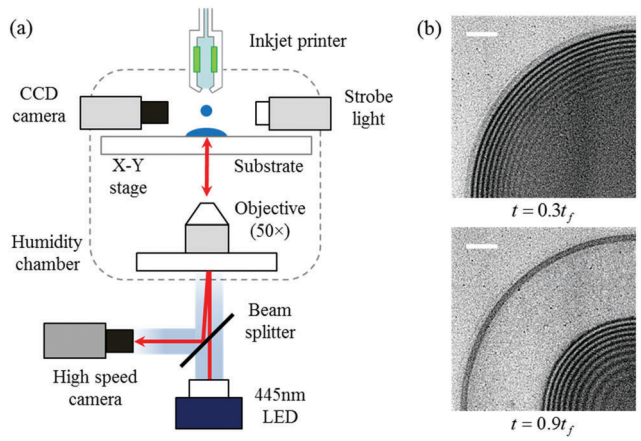

Fig. 1 (a) Schematic depiction of the interferometry technique for inkjet-printed drops. The dashed line represents the humidity-controlled chamber. (b) Interferometry images of an evaporating aqueous drop of 113 pL containing 20 nm carboxylate-modified particles at $t = 0.3t_f$ and $t = 0.9t_f$, where t_f is the total evaporation time. The initial particle volume fraction is 0.0025 and the relative humidity of the chamber is 35%. The scale bars represent 20 μm.

The ink was prepared by adding deionized water to 20 nm carboxyl (less hydrophilic, Invitrogen C37261) and carboxylate-modified (more hydrophilic, Invitrogen F8787) polystyrene nanoparticle suspensions to obtain a particle volume fraction of 0.0025. These nanoparticles are sulfate polystyrene particles, grafted with the carboxyl group. The ionization of the carboxyl group makes it more attracted to water molecules, thus responsible for the change of wettability. Carboxyl polystyrene nanoparticles[36] are charge-stabilized with a very low number of carboxyl groups present on the sulfate PS particle surface. Thus, the equilibrium contact angle for carboxyl PS particles is approximated to be the same as that of the sulfate PS particle of $\theta \approx 74°$.[37] But, carboxylate-modified polystyrene nanoparticles[36] are produced by copolymerizing carboxylic acid containing polymers grafted onto their already charged surfaces, which results in greater surface charge densities and higher hydrophilicity. The equilibrium contact angle for a carboxylate-modified PS particle was approximated as $\theta \approx 34°$ by comparing its surface charge density with existing measurements.[38] Note that these contact angle approximations are also based on the assumption that the particle wettability is not a strong function of the particle size.[37,39] The measured zeta potentials were −68.8 mV for carboxylate-modified particles and −37.4 mV for carboxyl particles, obtained by using a Zetasizer Nano (Malvern). The water and particle mixtures were then homogenized for 5 minutes in a sonicator (Cole-Parmer 8891) prior to printing.

The bottom-view interferometry imaging was conducted based on constructive (bright fringes) and destructive (dark fringes) interference resulting from the phase shift between the incident light reflected from the water–air and water–glass interfaces, respectively. The interferometry imaging setup consists of a 50× objective connected to an inverted microscope (Zeiss Axio Observer A1) illuminated by a blue (445 nm) high-power light-emitting diode (LED) (Thorlabs Solis-445C) and recorded at 10 000 frames per second with a resolution of 0.4 × 0.4 μm per pixel by a high-speed camera (Phantom V711). The captured interferometry images (Fig. 1b) were analyzed based on the well-known premise that the fringe-to-fringe spacing correlates to a local drop thickness differential of $\lambda/2$, where λ is the wavelength of the light source. The maximum measurable thickness is a strong function of the coherence of the light source used and for the LED (coherence length of 5.7 μm) used in this study, the maximum

measurable thickness was a few micrometers. The minimum measurable thickness depends on the wavelength of the light source and is $\lambda/4 \approx 111$ nm in the present study. With a temporal resolution of 100 μs, the interferometry technique allows for the instantaneous measurement of the drop thickness near the contact line and hence the contact angle from the linear fitting of ten nearest data points from the contact line. Once the contact angle is obtained, the full droplet profile is determined by the spherical cap fitting,[11] following $z = \sqrt{R^2/\sin^2\Theta - r^2} - R/\tan\Theta$, where z is the local droplet height, R is the contact line radius, r is the local radius, and Θ is the apparent drop contact angle. Note that, in this study, the Bond number $\mathrm{Bo} = \rho g d_0^2/\gamma < 0.005$, such that the gravitational effect on the drop shape is negligible. Here, ρ is the density of water, g is the gravitational acceleration, d_0 is the drop in-flight diameter, and γ is the surface tension of water. Fig. 1b shows the interferometry images of an evaporating aqueous drop containing 0.25% 20 nm carboxylate-modified particles at $t = 0.3t_f$ and $t = 0.9t_f$ (t_f is the total evaporation time), where well defined fringe patterns were observed close to the contact line. In addition, an optical profilometer (Zygo 7100) was used to analyze the deposition pattern *post-mortem*. As the high-speed interferometry tracked the instantaneous location of the contact line and the droplet shape, for each time frame, the contact line radius and droplet volume can be correlated with the *post-mortem* particle deposition profile at that contact line location. Combining *in situ* drop surface profile analysis and *post-mortem* deposition profilometry thus allows for the determination of the instantaneous particle volume fraction of the remaining colloidal drop and the time-dependent particle deposition rate.

3. Model for the number of particles required for pinning

To understand the effect of particle wettability on contact line pinning, a force balance analysis was conducted on the particles near the contact line, as shown in Fig. 2a, with the following assumptions:

(i) For picoliter-sized droplets, the particle Brownian motions are neglected close to the contact line where the particle Peclet number, $\mathrm{Pe} = 2R_{\mathrm{depo}}\nu_r/D_p \approx 8400$, is large. Here, $R_{\mathrm{depo}} \approx 110$ μm is the deposition radius of the droplet, $\nu_r \approx 0.91 \times 10^{-3}$ m s^{-1} is the velocity of the evaporation-driven outflow inside the just-printed sessile drop (evaluated at the contact line using eqn (3) with $\Theta \approx 6^\circ$ and $z \approx 10$ nm), and $D_p = k_B T/6\pi\eta r_p \approx 2.4 \times 10^{-11}$ m^2 s^{-1} is the particle diffusivity in water from the Stokes–Einstein equation,[40] where k_B is the Boltzmann's constant, T is the temperature, η is the dynamic viscosity of water, and r_p is the radius of the particle.

(ii) The contact line of the drop is initially pinned and the water–air interface during evaporation is presumably a spherical cap. Gravitational effects are neglected during evaporation since $\mathrm{Bo} = \rho g d_0^2/\gamma < 0.005$.

(iii) The evaporation process is assumed to be limited by vapor diffusion in air where the drop surface is assumed to be in phase equilibrium.[41]

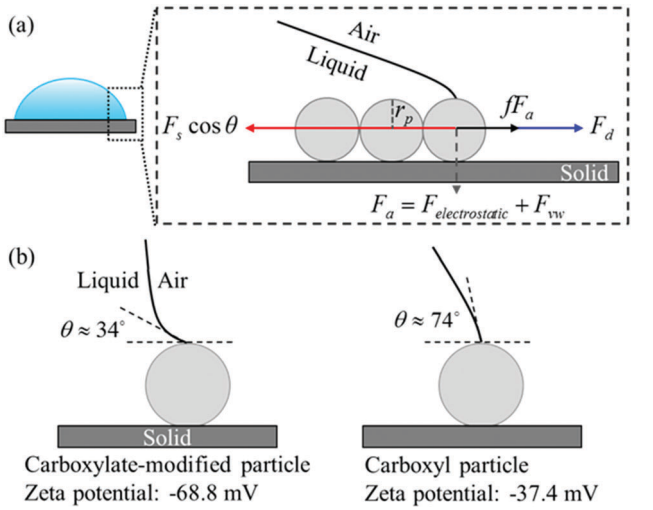

Fig. 2 (a) Schematic view of the surface tension (F_s), hydrodynamic drag (F_d), static friction (fF_a), and particle–substrate attraction (F_a) forces acting on particles near the contact line. (b) Schematic of the contact angle (θ) for the carboxylate-modified (more hydrophilic) and carboxyl (less hydrophilic) polystyrene particles at the triple-phase contact line.

(iv) Particles are initially considered to be uniformly distributed and dilute inside the printed drop. The van der Waals and electrostatic interactions between particles in the bulk of the droplet are not considered because the forces acting on one particle by the surrounding particles cancel each other such that the net effect is negligible. The non-DLVO forces acting on the particles are also neglected.

(v) The hydrodynamic drag force acting on the particles near the contact line is assumed to be constant considering that the velocity of the evaporation-driven outward flow does not vary significantly near the contact line (*e.g.*, the radial velocity reduces from 0.91×10^{-3} m s^{-1} to 0.21×10^{-3} m s^{-1} 5 μm away from the contact line). The change in drop viscosity due to particle packing near the contact line is ignored.

(vi) The surface tension force is acting on the partially wetted outmost particle of the pinned contact line with an air–water–particle contact angle θ shown in Fig. 2b. Monolayer particle assemblies on the substrate are assumed near the contact line for force calculations. In addition, the equilibrium and critical receding contact angles of the particle are assumed to be the same.

As shown in Fig. 2a, the horizontal component of the surface tension force acting on the particles near the contact line can be written as $F_s \cos\theta$, where F_s is the water–air surface tension force given as[42]

$$F_s = 2\pi r_p \sigma \quad (1)$$

Here, r_p is the particle radius and σ is the surface tension of the water–air interface.

The horizontal component of the hydrodynamic drag for a stationary particle inside the evaporating drop can be approximated by[42]

$$F_d = 6\pi r_p \eta \nu_r \quad (2)$$

where η is the dynamic viscosity of water and ν_r is the radial velocity of the evaporation-driven outward flow. Following the Hu–Larson model for a diffusion-limited evaporating droplet with a pinned contact line,[43] the radial velocity of the evaporation-driven outflow inside the sessile drop is given by

$$\nu_r = \left\{ -\frac{3}{8}\frac{1}{\tilde{r}}\left[(1-\tilde{r}^2) - (1-\tilde{r}^2)^{\Theta/\pi-1/2}\right] - \frac{\tilde{r}{z_0}^2\tilde{z}}{2{R_{depo}}^2}\left[\tilde{J}\left(\frac{1}{2} - \Theta/\pi\right)(1-\tilde{r}^2)^{\Theta/\pi-3/2}+1\right]\right\}\frac{R_{depo}}{t_f} \quad (3)$$

where $\tilde{r} = r/R_{depo}$ is the dimensionless radius, Θ is the apparent contact angle of the droplet, which can be experimentally measured from interferometry, $R_{depo} = \{\pi {d_0}^3/[3\pi\tan(\Theta/2)]\}^{1/3}$ is the droplet deposition radius, d_0 is the drop in-flight diameter, $\tilde{z} = z/z_0$ is the dimensionless drop height, z_0 is the initial drop height, $\tilde{J}(\tilde{r})$ is the local evaporation flux and $\tilde{J} = (t_f/\rho z_0)(1-\tilde{r}^2)^{\Theta/\pi-1/2}(Dc_v(1-RH)/R_{depo})(0.27\Theta^2+1.3)[0.6381 - 0.2239(\Theta-4/\pi)^2]$ is obtained from curve fitting numerical solutions of an evaporating pinned sessile drop.[43] Here, the total drying time $t_f = \pi\rho{R_{depo}}^2\tan(\Theta/2)/[8D(1-RH)c_v]$,[11,17] where D is the diffusivity of water vapor in air, c_v is the saturated vapor concentration, and RH is the relative humidity. The hydrodynamic drag for a stationary particle at the contact line can be evaluated by setting $r = R_{depo} - z/\tan(\Theta/2)$ with $z \approx 10$ nm (the particle radius) and using an experimentally measured drop wetting angle Θ.

The attraction force, F_a, between particles and the substrate can be calculated by[16,42]

$$F_a = F_{VW} + F_{electrostatic} \quad (4)$$

which includes both van der Waals and electrostatic interactions. The van der Waals force between particles and the substrate in a fluid medium is given by[44]

$$F_{VW} = 2nA_{123}{r_p}^3/[3Z^2(Z+2r_p)^2] \quad (5)$$

where n is the number of particles near the contact line, Z is the minimum separation distance between the particle and the substrate, and A_{123} is the Hamaker constant where the subscript 1 denotes the particle, 2 is the substrate, and 3 denotes the fluid medium. The electrostatic force between particles and the substrate in a fluid medium can be written as[45]

$$F_{electrostatic} = -2n\pi r_p\varepsilon\kappa[{\varphi_1}^2 + {\varphi_2}^2 - 2\varphi_1\varphi_2\exp(\kappa Z)]/[\exp(2\kappa Z) - 1] \quad (6)$$

where ε is the fluid permittivity, κ is the reciprocal of the Debye length, φ_1 is the zeta potential of the particles, and φ_2 is the zeta potential of the substrate. The static friction force arises due to this attraction force between particles and substrate and can hence be expressed as fF_a, where f is the friction coefficient that depends on the roughness of the contacting surface.[46,47] For particles of different wettabilities, the friction coefficient is assumed to be the same. In addition, the static friction force and the hydrodynamic drag are assumed to be independent and both contribute to the motion of the particles near the contact line.

Based on the balance of the surface tension, hydrodynamic drag, and static friction forces acting on particles near the contact line, the number of particles required for pinning, $n_{pinning}$, is hence given by

$$n_{pinning} = F_s\cos\theta/(F_d + fF_a) \quad (7)$$

Note that, as shown in Fig. 2b, the particle wetting angle θ is about 34° for carboxylate-modified (more hydrophilic) particles and 74° for carboxyl (less hydrophilic) particles.

Using eqn (1)–(7) with the property values provided in Table 1, the forces acting on particles near the contact line were estimated and the results are summarized in Table 2. Due to different particle wettabilities, the horizontal component of the surface tension force acting on the particles near the contact line is 1.26×10^{-9} N for carboxyl (less hydrophilic) particles and 3.79×10^{-9} N for carboxylate-modified (more hydrophilic) particles. The hydrodynamic drag force is 1.54×10^{-13} N for both types of particles. The attraction force between particles and the substrate is 3.0×10^{-10} N for carboxyl particles and 2.54×10^{-10} N for carboxylate-modified particles due to their different zeta potentials. For particles of different wettabilities, the change in the denominator of eqn (7), $F_d + fF_a$, is negligible because the hydrodynamic drag force, F_d, and the friction coefficient, f, are assumed to be independent of the particle wettability and the variation in the attraction force is very small. In addition, the water–air surface tension force, F_s, is independent of the particle wettability. Thus, the ratio of the number of particles

Table 1 Summary of parameters used in force calculations of evaporating aqueous colloidal drops containing polystyrene nanoparticles printed on glass

Symbol	Physical parameters	Value	Unit
A_{123}	Hamaker constant between particle and glass in water	3×10^{-20} (ref. 45)	J
c_v	Saturated vapor concentration in air	0.0232	kg m^{-3}
d_0	Drop in-flight diameter	60×10^{-6}	m
r_p	Radius of the particle	10×10^{-9}	m
ν_r	Radial velocity of the evaporation-driven flow at the contact line	0.91×10^{-3} (eqn (3))	m s^{-1}
Z	Minimum particle separation distance	0.4×10^{-9} (ref. 45)	m
ε	Permittivity of water	7×10^{-10}	F m^{-1}
η	Dynamic viscosity of water	0.9	cP
κ	Reciprocal of the Debye length	$(430 \times 10^{-9})^{-1}$ (ref. 45)	m^{-1}
ρ	Density of water	1000	kg m^{-3}
σ	Surface tension of water	0.072	N m^{-1}
φ_1	Zeta potential of polystyrene particles	−68.8 (carboxylate-modified) −37.4 (carboxyl)	mV
φ_2	Zeta potential of glass	−40 (ref. 45)	mV

Table 2 Forces acting on particles near the contact line of an inkjet-printed aqueous colloidal drop containing polystyrene nanoparticles on glass

Parameters	Carboxyl PS particles	Carboxylate-modified PS particles
$F_s \cos\theta$	1.26×10^{-9} N	3.79×10^{-9} N
F_d	1.54×10^{-13} N	1.54×10^{-13} N
F_a	3.0×10^{-10} N	2.54×10^{-10} N
$r_N = \frac{(n_{pinning})_{carboxylate\text{-}modified}}{(n_{pinning})_{carboxyl}}$	≈ 3	

required for pinning between the cases of carboxylate-modified (more hydrophilic) and carboxyl (less hydrophilic) particles can be given by $r_N = \frac{(n_{pinning})_{carboxylate\text{-}modified}}{(n_{pinning})_{carboxyl}} \approx \frac{\cos\theta_{carboxylate\text{-}modified}}{\cos\theta_{carboxyl}} \approx 3$. In other words, the number of particles required for pinning near the contact line increases 3 times when the particle wettability increases from a wetting angle of 74° to 34° while keeping the other parameters the same. The higher requirement for pinning of more hydrophilic particles presented here is consistent with the molecular dynamics simulation results of Li *et al.*,[48] which showed that the hydrophobic particle makes the contact line pinning easier than the hydrophilic one under the same substrate conditions.

4. Results

In order to understand the deposition morphologies of nanoparticles with different wettabilities, Fig. 3 shows the optical profilometry images of the deposition patterns of inkjet-printed colloidal drops containing 0.25% 20 nm carboxylate-modified (Fig. 3a, more hydrophilic) and carboxyl (Fig. 3b, less hydrophilic) nanoparticles, respectively, on a plasma-cleaned glass substrate with an in-flight drop diameter of 60 μm at a relative humidity of 35%. As shown in the zoomed-in images on the left, an outmost ring is observed for both cases, but a thicker ring of ≈0.06 μm thick and ≈5.2 μm wide is obtained for the more hydrophilic case (Fig. 3a) compared with that of ≈0.02 μm thick and ≈4.4 μm wide for the less hydrophilic case. In addition, at least five well-defined concentric inner rings of ≈0.02 μm thick are observed for the less hydrophilic case (Fig. 3b), which transitions into a spider web and foam-like deposition, while a spider web-like deposition is observed right next to the outmost ring for the more hydrophilic case (Fig. 3a). As shown in Fig. 3, a near hollow center is observed for both cases. Moreover, for the less hydrophilic case shown in Fig. 3b, the spacing of the concentric rings decreases from drop edge to the center.

The interferometry images at t/t_f = 0.06, 0.16, 0.5, 0.75, and 0.93 for evaporating aqueous colloidal droplets containing 20 nm carboxylate-modified (more hydrophilic) and carboxyl (less hydrophilic) nanoparticles are shown in Fig. 4a and b, respectively. The starting time (t = 0) is defined as when the inkjet-printed drop touches the substrate and the time at which evaporation is completed, t_f, is about 0.7 second, independent of the particle wettability. Thus, the particle wettability does not

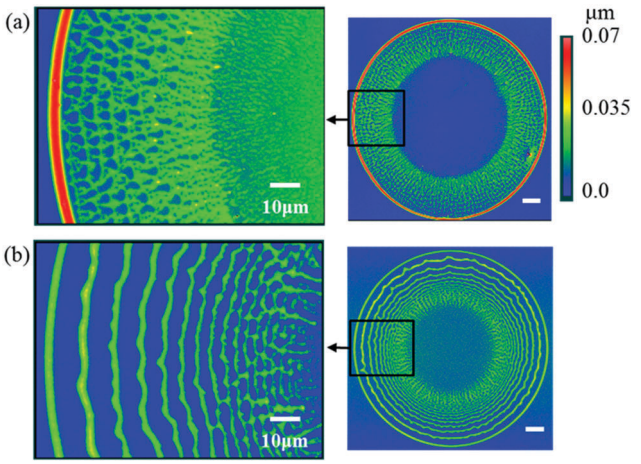

Fig. 3 Optical profilometry images of the deposition patterns on a plasma-cleaned glass substrate formed by inkjet-printed aqueous droplets containing (a) 20 nm carboxylate-modified (more hydrophilic) and (b) carboxyl (less hydrophilic) particles. The in-flight drop diameter of 60 μm is at a relative humidity of 35%. The particle volume fraction is 0.0025. The scale bars represent 20 μm in the two zoomed-out images of the right column.

have a noticeable influence on the evaporation rate of the droplets. Due to the highly symmetric nature of the deposition process, only a quarter of the drop is shown. For both cases, when the contact line is pinned between t/t_f = 0.06 and 0.16, the fringe spacing near the contact line slightly increases, which corresponds to a decrease in the local drop thickness and hence a decreaing contact angle. As the drop continues to evaporate, the contact line recedes from t/t_f = 0.16 to 0.5, 0.75, and 0.93, leaving behind a single ring for the more hydrophilic case but at least six well-defined concentric rings (including the outmost ring) for the less hydrophilic case. Comparing interferometry images of the same time frames, the contact line moves slower to the drop center for the more hydrophilic case where the fringe spacings are found to be slightly larger, indicating a smaller contact angle as compared to the less hydrophilic case. These *in situ* fringe patterns shown in Fig. 4 provide the instantaneous drop shape and direct evidence of how the deposition patterns are formed.

To understand the contact line dynamics of evaporating drops containing carboxylate-modified (more hydrophilic) and carboxyl (less hydrophilic) nanoparticles, Fig. 5a shows the normalized instantaneous drop radius, r/r_0, as a function of the normalized time, t/t_f, measured from the bottom-view images. For both cases, after the drop is in contact with the substrate at t = 0, the drop quickly spreads until it reaches the maximum diameter at around t/t_f = 0.06. The contact line is then pinned until t/t_f = 0.33 for carboxyl (less hydrophilic) particles and t/t_f = 0.39 for carboxylate-modified (more hydrophilic) particles. As shown in Fig. 5a, five noticeable stick-slip cycles, which correspond to the number of inner rings, can be observed for carboxyl particles from t/t_f = 0.33 to 0.72 with a longer stick time in the range of 0.047–0.070t_f as compared with the slip time of 0.010–0.025t_f. Similar stick-slip motions of the

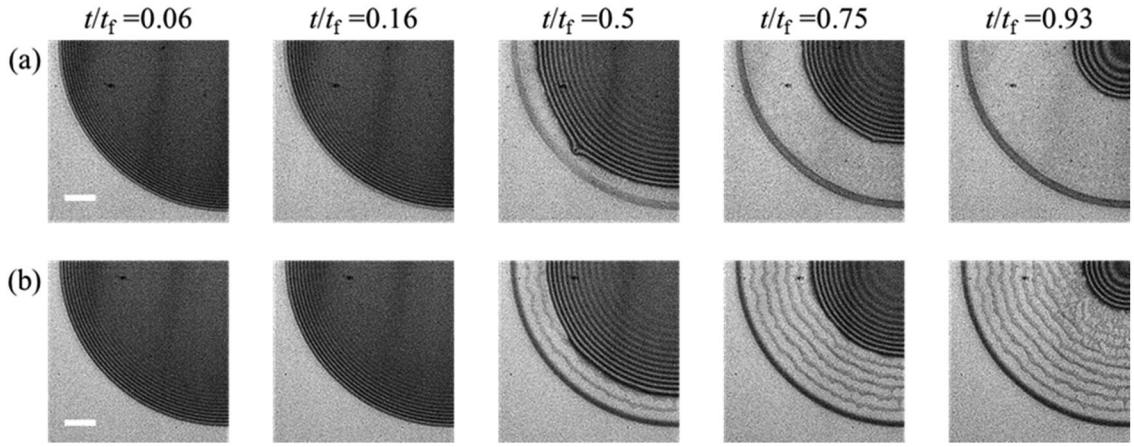

Fig. 4 Snapshots of interferometry images of inkjet-printed evaporating aqueous colloidal droplets on a plasma-cleaned glass substrate containing (a) 20 nm carboxylate-modified (more hydrophilic) and (b) carboxyl (less hydrophilic) nanoparticles. The experimental conditions are the same as in Fig. 3. The time at which evaporation is completed, t_f, is about 0.7 second, independent of particle wettability. The scale bars represent 20 μm.

contact line have been observed upon the evaporation of millimeter-sized drops for copolymer (particle contact angle, $\theta \approx 70^\circ$) and TiO_2 particles.[35,49] Unlike the carboxyl particles, continuous receding of the contact line was observed for the carboxylate-modified particle case once the contact line depins from the outmost ring. As shown in Fig. 5a, the contact line recedes slower for the carboxylate-modified particle case, possibly caused by the continuous deposition of particles (as shown in Fig. 3) slowing down the contact line speed. The experiments thus demonstrate the dependence of contact line dynamics on particle wettability.

To better understand the stick and slip behaviors of the contact line for colloidal drops containing carboxyl (less hydrophilic) particles, Fig. 5b shows the normalized stick and slip time as a function of the normalized drop radius, r/r_0, where the corresponding drop radius for the slip time is the average between two consecutive pinned positions of the contact line. A total of five stick-slip cycles were observed, where the stick time is found to be ~3–4 times longer than the slip time, both of which decrease as the drop radius decreases. Fig. 5c shows the normalized ring spacing, $\delta r/r_0$, *versus* the normalized drop radius, r/r_0, for carboxyl (less hydrophilic) particles, indicating that the ring spacing decreases from the drop edge to the center, in line with previous observations.[4,27] Good linearity is obtained for experimentally fitted $\delta r \sim r$, consistent with the model prediction[27] assuming a drop of spherical-cap shape before and after a slip motion on a hydrophilic substrate with negligible evaporation during slip.

To quantify the deposition morphology shown in Fig. 3, Fig. 6 shows the deposition profiles of inkjet-printed aqueous colloidal droplets containing 20 nm carboxylate-modified (more hydrophilic, Fig. 6a) and carboxyl particles (less hydrophilic, Fig. 6b) as a function of the normalized drop radius, r/r_0, on a plasma-cleaned glass substrate obtained from optical profilometry. For carboxylate-modified particles (Fig. 6a), about 34.1% of the particles are deposited in the outmost ring, while for carboxyl particles (Fig. 6b), the outmost ring contains about 16.5% of the particles and 16.0%, 9.7%, 7.0%, 6.7%, and 6.5% of the particles are found in the second, third, fourth, fifth, and sixth rings, respectively. Hence, the experimentally determined number of particles in the outmost ring is about two times higher for carboxylate-modified than carboxyl particles.

To better understand why the stick-slip motion of the contact line is observed for carboxyl (less hydrophilic) particles while the contact line continues to recede for carboxylate-modified (more hydrophilic) particles, the number of particles accumulated at the contact line during the experimentally measured stick time was determined. As shown in Fig. 7, when the contact line is pinned during the stick time t_s, the maximum distance travelled by the particles that finally accumulate at the contact line can be determined by $L_p = \int_0^{t_s} \nu_r dt$, where ν_r is the radial velocity of the particles determined by eqn (3). Here, in the ν_r calculations, we assume that the particles are flow tracers, the drop contact angle is the average value during the entire stick time, the radial position r of the particle changes with time, and the height position z is set to be the particle radius. The number of particles accumulated at the contact line can then be determined from the volume of the drop wedge within distance L_p to the contact line and assuming particles are uniformly distributed at 0.0025 volume fraction at the beginning of the stick time. Here, the volume of the drop wedge can be calculated by assuming a drop of a spherical-cap shape with a contact angle obtained from interferometry measurement, following

$$V_{wedge} = \frac{\pi}{2}\tan(\Theta/2)R_{depo}{}^3 - \pi L_p \tan\Theta\left(R_{depo} - L_p\right)^2 - \frac{\pi}{2}\tan\left[\sin^{-1}\left(\left(R_{depo} - L_p\right)/\left(R_{depo}/\sin\Theta\right)\right)/2\right] \times \left(R_{depo} - L_p\right)^3 \quad (8)$$

Note that Θ is the apparent drop contact angle, different from the particle wetting angle θ. This yields 9.21% of the particles available near the contact line for the outmost ring, and 1.47%, 1.33% and 1.24% for the second, third, and forth rings, respectively,

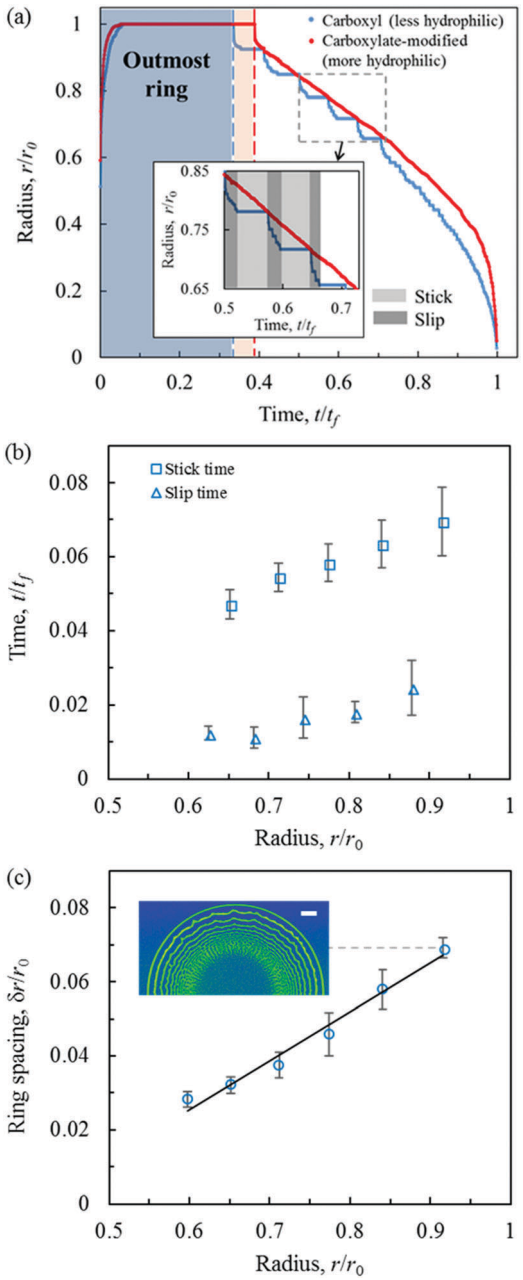

Fig. 5 (a) Normalized drop radius, r/r_0, as a function of the normalized time, t/t_f, measured from bottom-view images for 20 nm carboxyl (blue) and carboxylate-modified (red) particles, respectively, with the inset showing zoomed-in views of the stick and slip motions of the contact line. (b) Normalized stick (blue squares) and slip (blue triangles) times, t/t_f, as a function of the normalized drop radius, r/r_0, for 20 nm carboxyl particles. (c) Normalized ring spacing, $\delta r/r_0$, as a function of the normalized drop radius, r/r_0, for 20 nm carboxyl particles. The scale bar represents 20 μm. Error bars are obtained on the basis of three independent experiments. The outmost ring is not included in (b) and (c). The experimental conditions are the same as in Fig. 3.

for carboxyl (less hydrophilic) particles. Instead, about 13.6% of the carboxylate-modified (more hydrophilic) particles are available near the contact line for the outmost ring, 1.5 times higher than that of the carboxyl (less hydrophilic) particles, in qualitative agreement with the 2.1 times obtained experimentally.

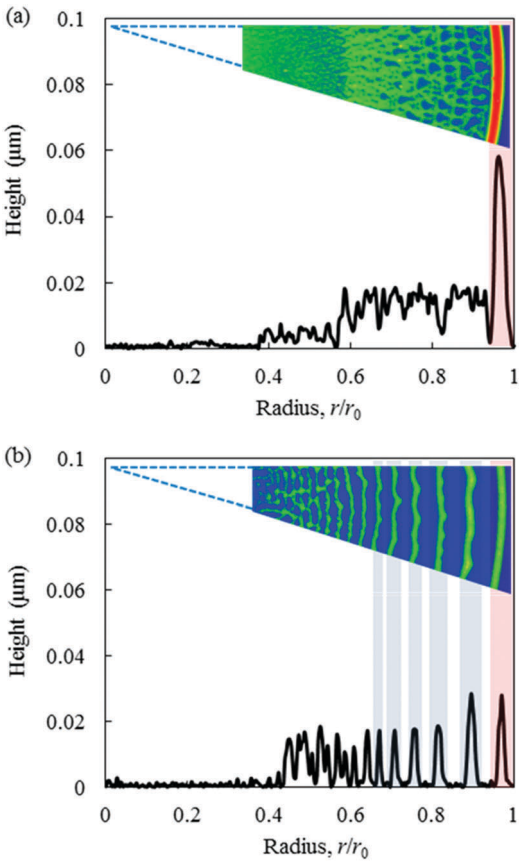

Fig. 6 Deposition profile as a function of the normalized drop radius, r/r_0, on a plasma-cleaned glass substrate formed by inkjet-printed aqueous droplets containing 20 nm (a) carboxylate-modified (more hydrophilic) and (b) carboxyl (less hydrophilic) particles. The experimental conditions are the same as in Fig. 3.

Meanwhile, for the carboxylate-modified (more hydrophilic) particles, after the outmost ring and assuming the same stick time as that of the carboxyl (less hydrophilic) particles, the results are 1.51%, 1.49% and 1.47% of particles available near the contact line for possible pinning during the second, third, and fourth stick time.

On the other hand, eqn (7) predicts the number of particles, n_{pinning}, required for pinning. The total number of particles required for pinning along the periphery of the drop contact line can be estimated by using $N_{\text{pinning}} = (2\pi R_{\text{depo}} n_{\text{pinning}})/(2r_{\text{p}})$, where R_{depo} is the instantaneous drop deposition radius and r_{p} is the particle radius. This allows one to compare the number of particles available and the number of particles required for pinning. If the number of particles required for pinning is smaller than the number of particles available, the contact line pins and particles form a ring and *vice versa*. For example, for carboxyl (less hydrophilic) particles, the number of particles required for pinning is always smaller than the number of particles available for any friction coefficient $f > 0.13$, which results in a pinned contact line. Whereas, for carboxylate-modified (more hydrophilic) particles, the number of particles required for pinning is always larger than the number of particles available when $f < 0.46$, resulting in continuous receding of

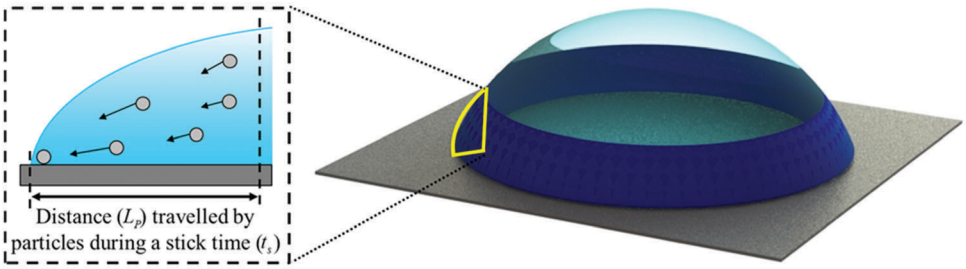

Fig. 7 Schematic showing the drop wedge within distance, L_p, to the contact line. Particles in this region can be advected to the contact line during the stick time.

the contact line. In other words, for the range of friction coefficient, $0.13 < f < 0.46$, the model agrees well with the experimental observations, *i.e.*, the stick-slip motion of the contact line and multiring deposition for the carboxyl particle case whereas the continuous contact line receding for carboxylate-modified particles.

Fig. 8a–d show the evolution of the drop volume, contact angle, particle number, and particle volume fraction of the evaporating colloidal drops containing carboxylate-modified (more hydrophilic) and carboxyl (less hydrophilic) particles, respectively. The instantaneous drop volume does not show an observable dependence on the particle wettability, similar to that observed by Anyfantakis *et al.*[34] Compared with the dotted linear line that starts at the end of spreading at $\sim 0.06t_f$ and ends when the drop fully evaporates at t_f, the evaporation is faster in the first half of the time but slows down in the second half, slightly different from the linear dependence of time as observed by others.[49,50] Fig. 8b shows that the contact angle initially starts at about 6° and decreases to about 4° for both cases during the constant contact area mode of evaporation when the contact line is pinned. The contact angle of the drop remains about 4° during the constant contact angle mode of evaporation before it decreases again during the final stage of evaporation where both the contact line and contact angle decrease. Changes of the contact angle during the stick-slip motion of the contact line (*i.e.*, t/t_f = 0.33 to 0.72) for carboxyl particles are not observable probably due to a very hydrophilic substrate where the contact angle may vary slightly within the error bars shown in Fig. 8b. During the entire evaporation, the contact angle for the carboxyl particle case is larger than that of the carboxylate-modified particles.

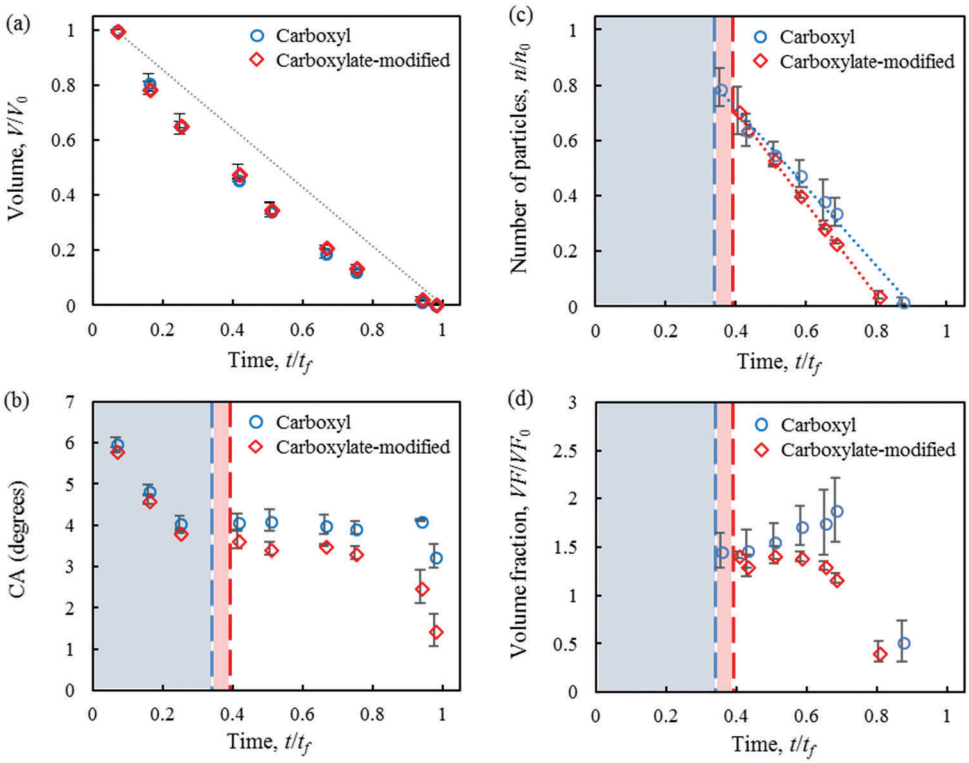

Fig. 8 Comparison of (a) the normalized drop volume, V/V_0, (b) the contact angle, (c) the normalized particle number, n/n_0, and (d) the normalized particle volume fraction, VF/VF_0, as a function of the normalized time, t/t_f, for drops containing 20 nm carboxylate-modified (more hydrophilic) and carboxyl (less hydrophilic) particles on a plasma-cleaned glass. The experimental conditions are the same as in Fig. 3. Error bars were obtained on the basis of three independent experiments. The blue dashed line represents the experimentally determined time to form the outmost ring for carboxyl particles and the red dashed line indicates that for the carboxylate-modified particles.

The number of particles remaining in the drop is then calculated by subtracting the particles already deposited by the time, t/t_f, from the total number of particles based on *post-mortem* optical profilometry. As shown in Fig. 8c, the number of particles remaining in the drop decreases linearly with time after the outmost ring for both carboxylate-modified (more hydrophilic) and carboxyl (less hydrophilic) particles, indicating constant particle deposition rates. In addition, a larger slope or a faster deposition rate is found for carboxylate-modified particles as compared to carboxyl ones, mainly due to the continuous deposition of particles as the contact line recedes. Moreover, more than 98% of the carboxylate-modified particles are deposited by t/t_f = 0.80 and that of carboxyl particles by t/t_f = 0.88, leaving near hollow deposition centers consistent with that previously shown in Fig. 6. Fig. 8d shows the instantaneous particle volume fraction of the remaining drop calculated from the remaining deposition volume, based on optical profilometry, divided by the remaining drop volume. It is shown that the particle volume fraction of the remaining drop first increases and then decreases with time for carboxyl particles, whereas for carboxylate-modified particles, the particle volume fraction monotonically decreases. After the outmost ring, the instantaneous particle volume fraction for carboxylate-modified (more hydrophilic) particles is always smaller than that of carboxyl (less hydrophilic) particles. However, more particles are required to pin the contact line for carboxylate-modified (more hydrophilic) particles based on eqn (7), which further explains why the stick-slip motion does not occur for more hydrophilic particles.

5. Conclusions

In this work, using combined *in situ* interferometry and *post-mortem* profilometry of inkjet-printed colloidal droplets, the effects of particle wettability on contact line dynamics and deposition patterns are examined. The stick-slip behavior of the contact line and the multiring deposition are observed only for colloidal drops containing carboxyl (less hydrophilic) particles where both the stick time and the ring spacing are proportional to the drop radius. A model is developed for the number of particles required for pinning based on the force balance of particles at the contact line. The number of particles required for pinning increases three-fold when the particle wettability increases from $\theta \approx 74^\circ$ to $\theta \approx 34^\circ$. After the outmost ring, the number of particles required for pinning is compared to the number of particles accumulated at the contact line during the stick time, resulting in enough carboxyl particles but not enough carboxylate-modified particles available for pinning due to their higher surface tension component, which in turn leads to continuous receding of the contact line over the deposited particles for the carboxylate-modified particle case. The results also show that the particle deposition rate is lower for carboxyl (less hydrophilic) as compared to carboxylate-modified (more hydrophilic) particles. The instantaneous particle volume fraction varies during drop evaporation and depends on the particle wettability. These findings will assist in the better understanding of materials printing processes for better control of deposition patterns.

Conflicts of interest

There are no conflicts to declare.

Acknowledgements

Support for this work was provided by the National Science Foundation under Grant No. CMMI-1401438 and CBET-1705745.

References

1 G. Reiter, Dewetting of Thin Polymer Films, *Phys. Rev. Lett.*, 1992, **68**(1), 75.
2 A. Oron, S. H. Davis and S. G. Bankoff, Long-Scale Evolution of Thin Liquid Films, *Rev. Mod. Phys.*, 1997, **69**(3), 931–980.
3 L. Frastia, A. J. Archer and U. Thiele, Dynamical Model for the Formation of Patterned Deposits at Receding Contact Lines, *Phys. Rev. Lett.*, 2011, **106**, 077801.
4 J. Xu, J. Xia, S. W. Hong, Z. Lin, F. Qiu and Y. Yang, Self-Assembly of Gradient Concentric Rings via Solvent Evaporation from a Capillary Bridge, *Phys. Rev. Lett.*, 2006, **96**, 066104.
5 C. N. Kaplan, N. Wu, S. Mandre, J. Aizenberg and L. Mahadevan, Dynamics of Evaporative Colloidal Patterning, *Phys. Fluids*, 2015, **27**, 092105.
6 Y. Mino, S. Watanabe and M. T. Miyahara, In Situ Observation of Meniscus Shape Deformation with Colloidal Stripe Pattern Formation in Convective Self-Assembly, *Langmuir*, 2015, **31**, 4121–4128.
7 Z. Lin and S. Granick, Patterns Formed by Droplet Evaporation from a Restricted Geometry, *J. Am. Chem. Soc.*, 2005, **127**(9), 2816–2817.
8 B. Li, W. Han, B. Jiang and Z. Lin, Crafting Threads of Diblock Copolymer Micelles via Flow-Enabled Self-Assembly, *ACS Nano*, 2014, **8**(3), 2936–2942.
9 B. Li, C. Zhang, B. Jiang, W. Han and Z. Lin, Flow-Enabled Self-Assembly of Large-Scale Aligned Nanowires, *Angew. Chem., Int. Ed.*, 2015, **54**(14), 4250–4254.
10 R. D. Deegan, O. Bakajin, T. F. Dupont, G. Huber, S. R. Nagel and T. A. Witten, Capillary Flow as the Cause of Ring Stains from Dried Liquid Drops, *Nature*, 1997, **389**, 827–829.
11 H. Hu and R. G. Larson, Evaporation of a Sessile Droplet on a Substrate, *J. Phys. Chem. B*, 2002, **106**(6), 1334–1344.
12 P. J. Sáenz, A. W. Wray, Z. Che, O. K. Matar, P. Valluri, J. Kim and K. Sefiane, Dynamics and Universal Scaling Law in Geometrically-Controlled Sessile Drop Evaporation, *Nat. Commun.*, 2017, **8**, 14783.
13 M. S. Bhamla, C. E. Giacomin, C. Balemans and G. G. Fuller, Influence of Interfacial Rheology on Drainage from Curved Surfaces, *Soft Matter*, 2014, **10**, 6917–6925.
14 C. C. Peng, C. Cerretani, R. J. Braun and C. J. Radke, Evaporation-Driven Instability of the Precorneal Tear Film, *Adv. Colloid Interface Sci.*, 2014, **206**, 250–264.

15 Ľ. Fraštia, A. J. Archer and U. Thiele, Modelling the Formation of Structured Deposits at Receding Contact Lines of Evaporating Solutions and Suspensions, *Soft Matter*, 2012, **8**, 11363–11386.

16 V. H. Chhasatia and Y. Sun, Interaction of Bi-Dispersed Particles with Contact Line in an Evaporating Colloidal Drop, *Soft Matter*, 2011, **7**, 10135–10143.

17 M. Pack, H. Hu, D.-O. Kim, X. Yang and Y. Sun, Colloidal Drop Deposition on Porous Substrates: Competition among Particle Motion, Evaporation, and Infiltration, *Langmuir*, 2015, **31**(29), 7953–7961.

18 D.-O. Kim, M. Pack, H. Hu, H. Kim and Y. Sun, Deposition of Colloidal Drops Containing Ellipsoidal Particles: Competition between Capillary and Hydrodynamic Forces, *Langmuir*, 2016, **32**, 11899–11906.

19 J.-H. Kim, S. I. Ahn, J. H. Kim and W.-C. Zin, Evaporation of Water Droplets on Polymer Surfaces, *Langmuir*, 2007, **23**(11), 6163–6169.

20 A. S. Sangani, C. Lu, K. Su and J. A. Schwarz, Capillary Force on Particles near a Drop Edge Resting on a Substrate and a Criterion for Contact Line Pinning, *Phys. Rev. E: Stat., Nonlinear, Soft Matter Phys.*, 2009, **80**(1), 011603.

21 G. McHale, S. M. Rowan, M. I. Newton and M. K. Banerjee, Evaporation and the Wetting of a Low-Energy Solid Surface, *J. Phys. Chem. B*, 1998, **102**(11), 1964–1967.

22 B. M. Weon and J. H. Je, Self-Pinning by Colloids Confined at a Contact Line, *Phys. Rev. Lett.*, 2013, **110**, 028303.

23 M. E. R. Shanahan, Simple Theory of ''Stick-Slip'' Wetting Hysteresis, *Langmuir*, 1995, **11**(3), 1041–1043.

24 E. Adachi, A. S. Dimitrov and K. Nagayama, Stripe Patterns Formed on a Glass Surface during Droplet Evaporation, *Langmuir*, 1995, **11**, 1057–1060.

25 R. D. Deegan, Pattern Formation in Drying Drops, *Phys. Rev. E: Stat. Phys., Plasmas, Fluids, Relat. Interdiscip. Top.*, 2000, **61**(1), 475–485.

26 X. Yang, V. H. Chhasatia and Y. Sun, Oscillation and Recoil of Single and Consecutively Printed Droplets, *Langmuir*, 2013, **29**(7), 2185–2192.

27 X. Yang, C. Y. Li and Y. Sun, From Multi-Ring to Spider Web and Radial Spoke: Competition between the Receding Contact Line and Particle Deposition in a Drying Colloidal Drop, *Langmuir*, 2014, **10**, 4458–4463.

28 S. Maheshwari, L. Zhang, Y. Zhu and H. Chang, Coupling Between Precipitation and Contact-Line Dynamics: Multiring Stains and Stick-Slip Motion, *Phys. Rev. Lett.*, 2008, **100**(4), 044503.

29 L. Zhang, S. Maheshwari, H. C. Chang and Y. Zhu, Evaporative Self-Assembly from Complex DNA-Colloid Suspensions, *Langmuir*, 2008, **24**(8), 3911–3917.

30 C. Seo, D. Jang, J. Chae and S. Shin, Altering the Coffee-Ring Effect by Adding a Surfactant-like Viscous Polymer Solution, *Sci. Rep.*, 2017, **7**(1), 500.

31 J. Xu, J. Xia and Z. Lin, Evaporation-Induced Self-Assembly of Nanoparticles from a Sphere-on-Flat Geometry, *Angew. Chem., Int. Ed.*, 2007, **46**(11), 1860–1863.

32 B. Li, W. Han, M. Byun, L. Zhu, Q. Zou and Z. Lin, Macroscopic Highly Aligned DNA Nanowires Created by Controlled Evaporative Self-Assembly, *ACS Nano*, 2013, **7**(5), 4326–4333.

33 J. Huang, R. Fan, S. Connor and P. Yang, One-Step Patterning of Aligned Nanowire Arrays by Programmed DipCoating, *Angew. Chem., Int. Ed.*, 2007, **46**(14), 2414–2417.

34 M. Anyfantakis, D. Baigl and B. P. Binks, Evaporation of Drops Containing Silica Nanoparticles of Varying Hydrophobicities: Exploiting Particle-Particle Interactions for Additive-Free Tunable Deposit Morphology, *Langmuir*, 2017, **33**, 5025–5036.

35 F. F. Shao, A. Neild and T. W. Ng, Hydrophobicity Effect in the Self Assembly of Particles in an Evaporating Droplet, *J. Appl. Phys.*, 2010, **108**, 034512.

36 https://www.thermofisher.com/us/en/home/life-science/cell-analysis/qdots-microspheres-nanospheres/idc-surfactant-free-latex-beads/high-activity-latex-beads.html.

37 V. N. Paunov, Novel Method for Determining the Three-Phase Contact Angle of Colloid Particles Adsorbed at Air - Water and Oil–Water Interfaces, *Langmuir*, 2003, **19**(13), 7970–7976.

38 N. Vogel, J. Ally, K. Bley, M. Kappl, K. Landfester and C. K. Weiss, Direct Visualization of the Interfacial Position of Colloidal Particles and Their Assemblies, *Nanoscale*, 2014, **6**(12), 6879–6885.

39 L. N. Arnaudov, O. J. Cayre, M. A. Cohen Stuart, S. D. Stoyanov and V. N. Paunov, Measuring the Three-Phase Contact Angle of Nanoparticles at Fluid Interfaces, *Phys. Chem. Chem. Phys.*, 2010, **12**(2), 328–331.

40 M. Wegener, N. Paul and M. Kraume, Fluid Dynamics and Mass Transfer at Single Droplets in Liquid/Liquid Systems, *Int. J. Heat Mass Transfer*, 2014, **71**, 475–495.

41 V. H. Chhasatia, A. S. Joshi and Y. Sun, Effect of Relative Humidity on Contact Angle and Particle Deposition Morphology of an Evaporating Colloidal Drop, *Appl. Phys. Lett.*, 2010, **97**, 231909.

42 J. Jung, Y. W. Kim, J. Y. Yoo, J. Koo and Y. T. Kang, Forces Acting on a Single Particle in an Evaporating Sessile Droplet on a Hydrophilic Surface, *Anal. Chem.*, 2010, **82**, 784–788.

43 H. Hu and R. G. Larson, Analysis of the Microfluid Flow in an Evaporating Sessile Droplet, *Langmuir*, 2005, **21**(9), 3963–3971.

44 M. Elimelech, J. Gregory, X. Jia and R. A. Williams, *Particle Deposition & Aggregation*, Butterworth Heinemann Publications, Woburn, MA, 1998.

45 T. Wong, T. Chen, X. Shen and C. Ho, Nanochromatography Driven by the Coffee Ring Effect, *Anal. Chem.*, 2011, **83**, 1871–1873.

46 M. Sahin, C. S. Çetinarslan and H. E. Akata, Effect of Surface Roughness on Friction Coefficients during Upsetting Processes for Different Materials, *Mater. Des.*, 2007, **28**(2), 633–640.

47 P. J. Blau, The Significiance and Use of the Friction Coefficient, *Tribol. Int.*, 2001, **34**(2001), 585–591.

48 Y. Li, H. Wu and F. Wang, Effect of a Single Nanoparticle on the Contact Line Motion, *Langmuir*, 2016, **32**(48), 12676–12685.

49 D. Orejon, K. Sefiane and M. E. R. Shanahan, Stick-Slip of Evaporating Droplets: Substrate Hydrophobicity and Nanoparticle Concentration, *Langmuir*, 2011, **27**(21), 12834–12843.

50 R. D. Deegan, O. Bakajin, T. F. Dupont, G. Huber, S. R. Nagel and T. A. Witten, Contact Line Deposits in an Evaporating Drop, *Phys. Rev. E: Stat. Phys., Plasmas, Fluids, Relat. Interdiscip. Top.*, 2000, **62**(1), 756–765.

